

VARIOUS TYPES OF ANTI-REFLECTIVE COATINGS (ARCS) BASED ON THE LAYER COMPOSITION AND SURFACE TOPOGRAPHY: A REVIEW

Majid Moayedfar¹ and Morteza Khalaji Assadi²

¹Faculty of Engineering and Technology, DRB-HICOM University of Automotive Malaysia, 26607 Pekan, Pahang Darul Makmur, Malaysia

²Department of Mechanical Engineering, Universiti Teknologi PETRONAS, 32610 Bandar Seri Iskandar, Perak Darul Ridzuan, Malaysia

Received: August 04, 2017

Abstract. One of the crucial factors in improving optical device performance is decreasing reflection, and enhancing light absorption or transmission from wide angles of incidence in a broad wavelength range. In this regard, efficient anti-reflective surfaces demonstrating multi-functional capabilities and showing prospective quasi-omnidirectional anti-reflective and broadband properties are proposed. The selection of a suitable coating material is a key factor in reducing reflection on these surfaces. Hence, this review aims to outline the inception of durable and inexpensive ARC materials that can be applied in different electronic and optical equipment, based on its original conceptualization. Strategies to reduce reflectance will be discussed, and various forms of ARC investigated, paying attention to layer composition and surface topography. To conclude, among all available ARC materials, a 2D rectangular grating for light absorption on GaSb surfaces showed superior properties.

1. INTRODUCTION

Light reflection occurs on a variety of surfaces between two mediums that have distinct refraction indices. Hence, when two refraction indices are closer, less light will be reflected. However, no reflection will occur if the reflection index of the coating materials is similar to that of the surrounding air [1-3]. Generally, when the incidence angle is far from normal, there will be increased light reflection on a surface [2]. The angle where there is nonpolarized light reflection is known as Brewster's angle and its range depends on the refraction indices of two mediums [4-8].

The constantly growing demand for optoelectronic and optical equipment in diverse areas, including consumer electronics and space exploration has created the need to identify the best ways to im-

prove the efficiency of light collection. In this regard, the use of anti-reflective coatings on the glass covers of solar panels' has been effective as it was proved to provide better glare reduction and transmission [9,10]. In terms of solar cells, silicon nitride or titanium dioxide coatings in nano scales are used to reduce reflectance. Moreover, light coupled into the cell can be increased through the use of a textured front surface of the solar cells particularly in mono-crystalline silicon. Meanwhile, the low conversion energy generated as a result of reflection is further reduced in conventional photovoltaic components; this hinders the shift to alternative energy sources such as nuclear power [11,12].

The rapid advancement of modern optoelectronic devices including super-compact cameras, touchscreens, and displays has created new de-

Corresponding author: Morteza Khalaji Assadi, e-mail: morteza.assadi@utp.edu.my

mands on the ARC industry. There are three features required by the current optic market: broadband, non-iridescence or the insensitivity to the angle of incidence, and products being ultrathin [1,8,13].

The improper selection of the material and limited understanding of their specification as ARCs will lead to higher reflection, less transmission and correspondingly the efficiency of the solar cells. Therefore, this study aims to review the most common and practical ARC material categorized with respect to their layer composition in two amounts of layers (single-layer, double-layer, multi-layer and gradient refractive index in Section 2), and layers distribution (homogeneous or inhomogeneous in Section 3), and surface topography (Section 4). It should be mentioned that in the material introduction and investigation, the application of solar cells was highlighted and given more consideration.

2. LAYER COMPOSITION (NUMBER OF LAYERS)

2.1. Single-layer ARCs

The Fresnel Equation can be used to calculate the intensity of light reflecting on each surface representing any medium's interface with the neighboring environment. Here, n_s represents a non-absorbing material through the refractive index at an ideal wavelength. In this regard, to decrease the substrate reflection down to zero at that wavelength, the coating thickness should achieve the subsequent circumstances [1,14]:

$$n_{arc} = \sqrt{n_s \cdot n_{env}}, \quad (1)$$

$$d_{arc} = \frac{\lambda}{4 \times n_{arc}}, \quad (2)$$

where n_{env} and n_{arc} are the refractive index (RI) of the medium and ARC surrounding respectively, and d_{arc} is the ARC thickness.

It should be noted that these equations are valid only for a nonabsorbing, homogeneous medium, else, the loss of each medium will make the calculation more complicated [15,16]. The biggest challenge for single-layer with quarter-wavelength ARCs is the decrease in the reflectivity for partial wavelengths and incidence angles, where they will vanish at glazing incidence angles. This is because of the varying incident light optical path-lengths of the glazing incidence. In this light, the phase difference between the the incident and reflected waves can-

cel each other out when the glazing incidence is dependant on the norm [17-19]. Furthermore, it is difficult to find any material in low RI single-layer ARCs transparent surface, which usually have less RI substrates. For example, the ideal RI of coating for 550 nm wavelength should be 1.22 for glass ($n = 1.5$), which is not possible in nature. Consequently, glass should be replaced with a material with an RI similar to that of glass, which might not be able to decrease the reflection efficiently. A possible solution to this problem is reducing reflection by the creation of micro or nano-structures on the Si substrate [7,14,20-22].

In recent years, there have been several successful applications of TiO_2 nano structures based ARC on solar cells. Shi et al. (2013) reported that when the Graphene /Silicon (G/Si) solar cell is in use, TiO_2 ARC and HNO_3 doping had the power conversion efficiency, commonly known as PCE, of 14.6% [8]. In this case, the combination of the interfacial oxide layer engineering TiO_2 ARC and AuCl_3 can boost the PCEs of Graphene /Si solar cell doping technique to the reach the maximum conversion efficiency of 15.6% [23].

One of the best candidates for single layer ARCs is inorganic coating layers similar to polymers [24]. On the other hand, there have been limited investigations into the use of polymer optical coatings in optoelectronic applications; despite the fact that polymers that have high refractive indexes, such as polystyrene with $n \sim 1.6$ [26,26] and poly methyl methacrylate (PMMA) with $n \sim 1.5$ [24] they are transparent to visible light. Even though they demonstrate lower refractive indices in comparison to inorganic ARCs, polymer coatings are stretchable, lightweight, and bendable; hence, despite their simple fabrication process, the results are significant. Therefore, some researchers have considered the use of polymer on a substrate like graphene, for instance, to decrease the reflection. One typical example of this application is the Xin Gan et al. (2016) study that applied polymer PMMA as a single layer ARC on a layer of graphene to decrease the reflection (Fig. 1a) [27]. Although the fabrication process of this coating is simple, the results are considerable.

Based on the common graphene transfer process, the graphene was spin-coated with PMMA ($Mw \approx 50000 \text{ mol g}^{-1}$, 4 wt.% in ethyl lactate) at a particular speed (e.g. 1000-3000 rpm). As a result, the copper substrate underneath the graphene film was etched away from the FeCl_3/HCl solution, resulting in the PMMA-coated graphene floating on

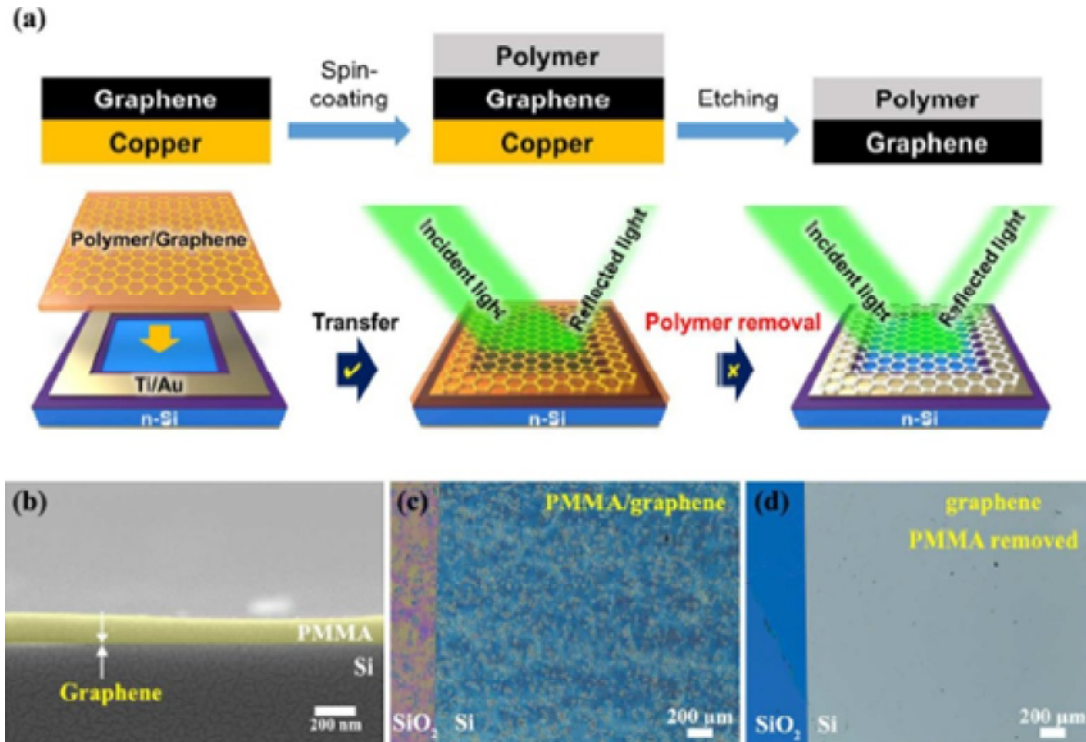


Fig. 1. (a) Schematic view of polymer-coated G/Si solar cells fabrication. (The copper substrate underneath the graphene film was etched away in FeCl_3/HCl solution) (b) The cross section of G/Si with PMMA coating from Scanning electron microscope (SEM) of (2000 rpm, $M_w \approx 50,000 \text{ mol g}^{-1}$, 4 wt.% in ethyl lactate). False colour (yellow) is applied on PMMA layer. Cracks on the surface of Si were caused by inhomogeneous deposition of Au coatings, which are necessary for the SEM characterization of PMMA layers. Optical microscope images of G/Si solar cells (c) with PMMA coating (2000 rpm) (d) without PMMA layers. Reprinted with permission from X. Gan, R. Lv, H. Zhu, L. P. Ma, X. Wang and Z. Zhang // Journal of Materials Chemistry A4 (2016) 13795.

the water surface. A planar and patterned silicon wafer with back on top was used to 'retrieve the final polymer-coated graphene from the water. Ti/Au electrodes (see Fig. 1a) was used to form G/Si heterojunction solar cell device right after the etchant residue had been washed away with ultrapure (UP) water and SC-2 solution ($\text{HCl}/\text{H}_2\text{O}_2/\text{H}_2\text{O} = 1:1:10$, v/v). The cross-section image of a G/Si solar cell with PMMA coating (spun at 2000 rpm) obtained from the scanning electron microscope is illustrated in Fig. 1b. The region in Fig. 1b illustrates the PMMA thickness layer, which was measured at 125 to 137 nm. Meanwhile, Figs. 1c, 1d, and 1e illustrate the images from the optical microscope [27]. The morphology of PMMA-coated graphene on silicon was demonstrated for the PMMA-coated G/Si devices with spinning rates of 1000, 2000, and 3000 rpm, the average thicknesses of PMMA coatings were 134, 108, and 89 nm, respectively. It was observed that both thickness and roughness of the polymer coatings were reduced at higher spinning rates. In the same study by Xin Gan et al. (2016), the thick-

ness of polymer protective coatings, light absorption and short-circuit current density of graphene solar cells were greatly enhanced [27]. Therefore, the PCEs can rise to 13.34% when the HNO_3 doping has been applied on PMMA-coated G/Si solar cells using this method.

2.2. V-coating (double-layer ARCs)

It is possible to employ the double-layer ARCs, in order to decrease zero reflectance. The proceeding equation shows the necessary index condition for a double-layer coating with similar optical thickness ($n_1 d_1 = n_2 d_2 = \lambda/4$), as shown [28]:

$$\frac{n_1}{n_2} = \sqrt{\frac{n_0}{n_s}} \quad \text{or} \quad n_1 n_2 = n_0 n_s. \quad (3)$$

The coating's profile is normally in a V-shape layer, hence, they are called v-coatings [29] similar to quarter-quarter coatings referring to their thickness. For laser applications, it is claimed that the

V-coatings could offer the best solution as this process requires minimum reflection only at specific wavelengths. At the same time, resistance to severe laser radiation is also significant [28,30]. In regards to double-layer ARCs, the upper film fronting the air normally shows the lowest RI, while layers below this are successively sequenced in ascending order on the basis of their refractive indices. The double-layer ARCs should fulfill the interference requirements to effectively eliminate the active back waves from the substance surface, the interference. Thus, each individual single layer thickness is normally set at quasi or quarter of the active wavelengths of $\lambda/2$ and $\lambda/4$ [31].

Meanwhile, the outdoor solar panels experience two layers of reflection; the first is at the cover layer of the glass, while the second is on the surface of Si-PV. Researchers have undertaken studies using single-layer thin CeO_2 (RI=2.2) SiO (RI = 1.85), and ZnS with RI = 2.3 films on Si substrate; following this, for V-coatings, MgF_2 (RI = 1.38) as the exter-

nal layer and CeO_2 ($n = 2.2$), SiO ($n = 1.85$), and ZnS ($n = 2.3$) as the inside layer on Si with reflective index of 3.5- 4 at 400 -1100 nm wavelength [32]. Table 1 illustrates research discoveries pertaining to various double layer ARCs.

Magnesium fluoride (MgF_2) with an RI of 1.38 is used most frequently. As a result, the BK7 glass surface reflectance was decreased to less than 1.3% from approximately 4% at the normal incidence and center wavelength specified. Although single-layer MgF_2 has a broad usable wavelength zone, it somewhat lacks the performance required [28].

In L. Lancellotti et al. (2016), Schottky barrier solar cells with graphene/n-silicon were made from several layers of graphene film which were produced using chemical vapor deposition (CVD) before being shifted onto silicon wafers made of n-type crystalline [39]. The study examined the Graphene/n-Si solar cells and studied the effects of the deposition of double-layer antireflection coating (DARC) with magnesium fluoride/zinc sulphide (MgF_2/ZnS) on the

Table 1. Some research discoveries pertaining to various double layer ARCs.

Ref	Year	Materials	Description
[33]	2000	$\text{MgF}_2/\text{CeO}_2$	DLAR coating, which has been theoretically optimized was reported to have the minimum average reflectance of 1.87% , with the range of wavelengths between 0.4 μm to 1.1 μm .
[32]	2002	SiO , CeO_2 and ZnS	Compared to single-layer coatings, the double-layer coatings were found to produce a low reflectance region that was significantly broader.
[34]	2005	silicon nitride (SiN) and silicon oxide	Based on the AM1.5 photon flux (300-1150 nm), the SiO_2 and SiN and showed the best combination, with reflectance index of 0.044.
[35]	2006	$\text{MgF}_2/\text{SiN}_x$	The study produced Silicon solar cells with conversion efficiency of 16% through by using a conventional solar cell fabrication line.
[36]	2013	Al_2O_3 and TiO_2	Compared with the designed 0.408%, in practice, the average reflectance is 0.535% (400~680nm),
[37]	2014	$\text{SiO}_2/\text{TiO}_2$	The study measured the DLAR reflection spectrum, resulting in the least reflection about 2.3% in 630 nm and the mean reflection of 7% (400-1000)
[38]	2015	mesoporous silica and nano porous silica	The broadband AR coating maximum transmittance was estimated to surpass 99.6% in the visible area (400 to 800 nm), and as 100.0% at the peak value.
[39]	2016	MgF_2/ZnS	The combined impacts of graphene doping and anti-reflection treatment have made possible for the efficiency of power conversion to reach 8.5%. This exceeds the undoped and plane device performance, reflecting a pristine performance by a factor of 4.
[40]	2017	$\text{TiO}_2/\text{SiO}_2$	Double-layer ARC provides a 14.54 mA/cm^2 gain in the photocurrent.

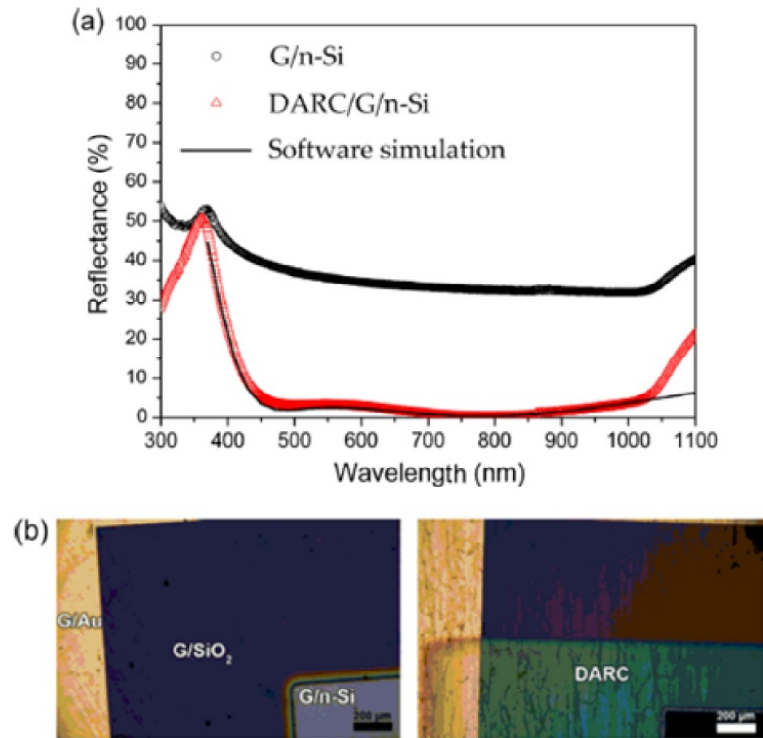


Fig. 2. (a) The spectra of light reflection observed on a G/n-Si structure prior (black circles), the Essential Macleod software modelling (red triangles) and the continuous line as after the DARC evaporation. (b) Microscopic images of a fraction on the front side of the device prior (left), the deposition of DARC (right). Reprinted with permission from L. Lancellotti, E. Bobeico, A. Capasso, E. Lago, P. D. Veneri and E. Leoni // *Solar Energy* **127** (2016) 198.

top of a device. This coating was commonly applied in solar cells with Si bases because of their low absorption through the visible area and suitable refractive indexes [39]. In this light, with regards to maximum antireflection result, the coating with MgF₂/ZnS allowed influential light reflection spectra of structures with DARC/G/n-Si and G/n-Si (Fig. 2a).

This illustrates the ideal relationship between the simulated and experimental reflectance spectra for wavelengths below 1000 nm. Fig. 2b shows optical microscope images from the top view of the device before and after the deposition of DARC [39]. This showed the permeability of DARC to nitric acid vapor and it was observed that this treatment did not affect its optical attributes and illustrated a stable result over time.

2.3. Multi-layer ARCs

The multilayer ARCs were calculated as the researcher began to focus on the broadband anti-reflection (BAR). On the other hand, researchers often face difficulties in the overall reflectivity and the tradeoff between a larger bandwidth. Thus, the mathematical analysis of multilayer ARCs extends the

previous destructive interference type vector model [28,41]. Hence, the overall reflected vectors summation must be minimized. This was carried out by making an adjustment to the film thickness and the RI. A computational study on this issue has shown that the inserting an additional Si layer in the middle of the low index and high index of SiO₂ to create the blue transitivity of approximately 96% (at 480 nm), which is the maximum. Similarly, alternate high and low RI layers in biological species like Coleoptera could cause optical interference. Table 2 summarizes the other research observations from multilayer ARCs research based on the efficiency, transmittance and reflection.

2.4. Gradient refractive index ARCs

The RI profile's gradients of RI coatings differ based on the range of curves- linear, cubic, parabolic, Quantic exponential-sinusoid and exponential to adhere to the Rayleigh effect. Southwell presented a gradient ARCs where the equations govern different gradient refractive index (GRIN) as shown below [46], where, reflective index of incident medium, such as air, is n_i and RI of the substrate is n_s :

Table 2. A summary of multilayer ARCs achievements.

Ref	Year	Materials	Description
[42]	2015	GaAs _{0.69} P _{0.31}	The study is showed that the optimized double- and triple-layer ARCs are able to decrease reflectance to 5% when the spectral range is between 400–945 nm. The latter maintains this performance at a higher level than the broader spectrum of 390–1000 nm, in comparison to 25–45% reflectance in a bare solar cell.
[43]	2012	(SiO ₂) _x (TiO ₂) _{1-x}	A decreased total reflection (43% to 28%) shows the optimized 4-layer antireflection coating which causes the high conversion efficiency incident of -photon-to-electron
[44]	2016	ZrO ₂ -polymer composite/spray-deposited TiO ₂ -compact multilayer	The cell conversion efficiency has improved by a factor of 0.8% (from 15.19% to 15.88%) as the multilayer ARC. J_{sc} was enhanced further by 2 mA cm ⁻² (from 35.3 mA cm ⁻² to 37.2 mA cm ⁻²) compared to a single TiO ₂ -compact ARC.
[45]	2015	high-density polypropylene(HDPE)	A ten-layer AR coating was designed for widely used silicon wafers. The AR coatings comprise of double-side integrated with a 375-μm-thick silicon wafer, which could enhance the overall THz transmission by 95.00% (114.46% bandwidth) from 0.250 THz to 0.919 THz.
[31]	2013	SiO ₂ /ZnS	This study presents the SiO ₂ /ZnS double-layer ARC theoretical optimization of the on the AlO ₃ ; here, the .5P window layer for double- and triple-junction SCs was under AM1.5. For the double-junction SC, the changes in ARC thickness and average reflectivity were determined to be less than 2 nm and 0.07%, respectively

Linear index profile,

$$n = n_i + (n_s - n_i)t, \quad 0 \leq t \leq 1, \quad (4)$$

Cubic index profile,

$$n = n_i + (n_s - n_i)(3t^2 - 2t^3), \quad (5)$$

Quantic index profile,

$$n = n_i + (n_s - n_i)t(10t^3 - 15t^4 + 6t^5). \quad (6)$$

Chao Xiong et al. (2017) reported a new design of graded refractive index antireflection coatings for silicon solar cells [47]. Here, the matrix method was used to simulate the reflectance spectrum of the nanoporous silicon dioxide (SiO₂) layer/SiO₂/gradient index SiO_xN_y/gradient index PS (or other black silicon) multilayer ARCs. In comparison to the SiO_xN_y/gradient index PS (or other black silicon) double gradient index layer ARC, the reflectance spectrum of this novel ARCs is lower, which is in the range of 430–1200 nm [47]. Meanwhile, this new ARC illustrates a low reflectance ($\leq 2\%$) in a relatively broad spectrum compared to double-layer SiO_xN_y/PS ARCs. This new nano porous silicon dioxide (SiO₂) layer/SiO₂/gradient index SiO_xN_y/gra-

dient index PS (or other black silicon) multilayer ARCs could be applied in Silicon photovoltaic solar cells. Table 3 summarises findings from various studies on gradient refractive index (GRI) ARCs based on efficiency, transmittance and reflection.

Furthermore, Minkyu Choi et al. (2015) produced the MgF₂/SU8 MCs/Si which comprises of the gradient index material structures, this was produced through soft imprint lithography which uses the sapphire master molds that contain 2 dimensional (2D) periodic hexagonal conical micro grating pattern arrays [50,54]. In order to investigate their surface wetting behavior in comparison to both bare Si and their SU8 MCs/Si, anti-reflective properties were theoretically and experimentally tested. MgF₂ film coating on structures of SU8 MCs/Si caused a decline in the amount of reflection, this enhanced the transmission of diffused lights. Moreover, a super hydrophilic media ($\theta_c < 10^\circ$) was observed in the sample, namely, MgF₂/SU8 MCs/Si with the wavelengths of 350–1100 nm (i.e., $R_{avg} < 15.1\%$ and $R_{sw} < 13\%$ for the SU8 MCs/Si and $R_{avg} < 38.5\%$ and $R_{sw} < 38\%$ for the bare Si). This lead to reduced values for mean of reflectance (R_{avg}), there were observed at

Table 3. A summary of gradient refractive index ARCs achievements.

Ref	Year	Materials	Description
[47]	2017	gradient index SiO _x N _y /gradient index porous silicon	This ARCs has a lower reflectance in 430–1200 nm range. Compared to double-layer SiO _x N _y /porous silicon ARCs, this novel ARC has a low reflectance ($\leq 2\%$) in a relatively broad spectrum
[48]	2017	gradient index p-type amorphous silicon oxide (p-SiO _x)	Single-layer and double-layers of p-SiO _x ARCs with GRI are investigated experimentally and theoretically. The composite p-SiO _x thin films not only decrease optical reflectance, but also improve electrical conductivity. The minimum average reflectance of 10% is obtained in broader wavelength range.
[49]	2016	silicon oxide thin film with GRI	The minimum average reflectance of 10% is obtained in broader wavelength range.
[50]	2015	gradient index magnesium fluoride (MgF ₂) film-coated SU8 ultraviolet curable polymer	The MgF ₂ /SU8 MCs/Si specimen had a superhydrophilic surface ($\theta_c < 10^\circ$) and at wavelengths of 350–1100 nm showed lower R_{avg} around 14% and R_{sw} values near 12.1%.
[51]	2015	ZnO nanorods (NRs) and TiO ₂ layers	The ZnO NRs/ TiO ₂ layer exhibits in a low average of wavelength, the reflectance of 6.00% in an extensive spectral range of $\lambda=380-1800$ nm.
[52]	2016	graded-index layers LaF ₃ , PrF ₃ , ErF ₃ , and SmF ₃ , admixed by a diverse quantity of BaClF	An effective RI near 1.2 obtained that is less than those of infrared low-index coating materials used generally.
[53]	2014	gradient index aluminum-doped zinc oxide	When this material is applied to an active solar device, the power conversion efficiency of the solar cell is raised to 10% at the angles of 10° or higher.

around 14% and the solar weighted reflectance (R_{sw}) around 12.1%. In addition, significant light diffraction with a H_{avg} value of near 89.8% in a wide wavelength range between 350 to 1100 nm was evident [50]. Consequently, these findings have demonstrated an insight into the broadband wide-angle antireflection microstructures. This can be simply produced using cheap, soft lithography, which has significant diffuse light scattering properties and super hydrophilic cleaning functions that can be used to fabricate optoelectronic devices based on high-performance Si.

3. LAYER COMPOSITION (LAYERS DISTRIBUTION)

3.1. Homogeneous ARCs

RI and thickness limitations could be used to impose the single homogeneous layer of the refractive index (n). In this light, RI must adhere to $n = \sqrt{n_{air} n_s}$

and have a thickness of $\lambda/4$ [55,56]. Meanwhile, n_{air} refers to unity and n largely depends on n_s when the substrate is surrounded by air. Figs. 3a-3c presents the homogeneous ARCs including single layer, multilayer and patterned layer.

A pattern or porous layer will considerably decrease the (n), and facilitate the matching of the optical impedance (Fig. 3b). Furthermore, in a homogeneous setup, multiple thin layers would result in no reflectance in a particular wavelength (s) [28].

3.2. Inhomogeneous ARCs

The varying RI from n_{air} to n_s would progressively further reduce the contribution to reflection from interfaces [52,58,59]. In this case, the overall layer thickness is not significant [57] from the design perspective, even though the thickness should surpass λ_u or $2\lambda_u$, where λ_u represents the incident light upper wavelength [60]. Figs. 3d-3f illustrates the inhomogeneous ARCs for single layer, multi-layer

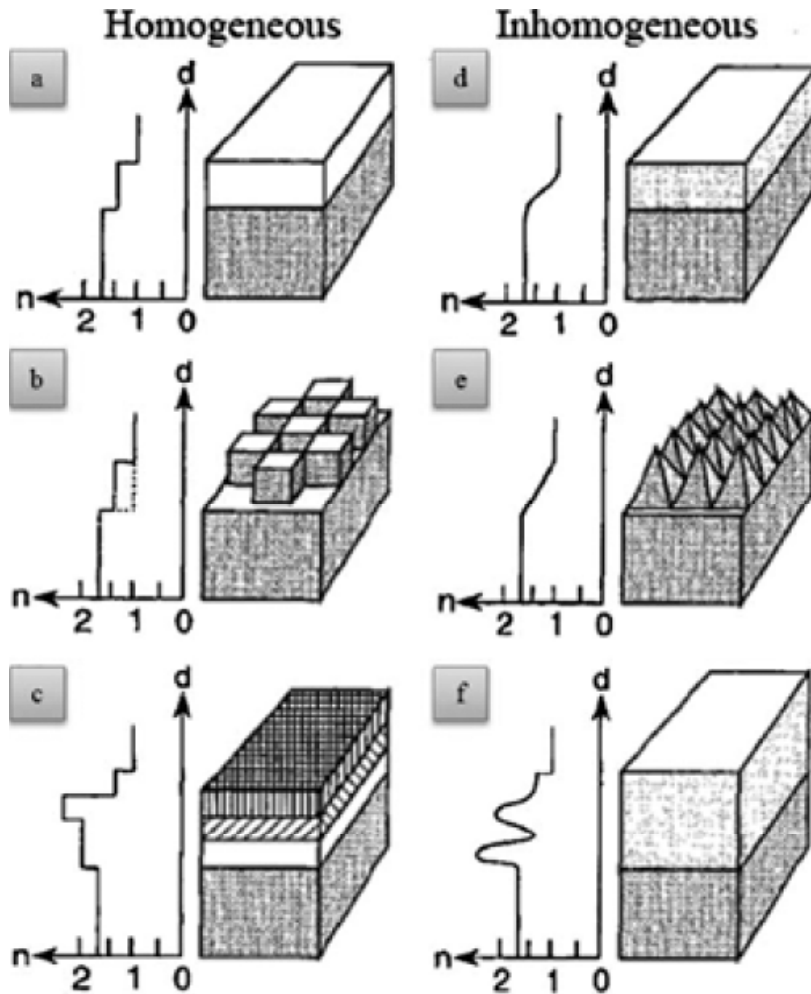


Fig. 3. Single layer Homogeneous ARCs, (a), patterned Single layer Homogeneous ARCs (b) multilayer Homogeneous ARCs (c) single inhomogeneous layer ARC (d), patterned single layer inhomogeneous ARC (e) multi-layer inhomogeneous ARC (f). The variation in refractive index in regards to the thickness of the film. Reprinted with permission from J. Dobrowolski, D. Poitras, P. Ma, H. Vakil and M. Acree // *Applied optics* **41** (2002) 3075.

and patterned layer. These inhomogeneous ARCs can be predicted using the large sub-layer's number where there is a very small RI difference between the adjacent sub layers (Fig. 3f). Moreover, by considering $n_{\text{air}}=1$, zero reflectance can be provided by the inhomogeneous layer when the layer thickness adheres to the λ_u limit and the sub wavelength structure is incorporated into the layers [28] as shown in Fig. 3f.

4. BASED ON THE SURFACE TOPOGRAPHY

This ARC was developed in accordance with the omnidirectional AR properties and the need to retain the broadband AR. It can be categorized as porous, Biomimetic photonic nanostructures, textured surface and Anti-reflection grating.

4.1. Porous ARCs

Numerous research has been conducted in this area, particularly regarding porous silicon (PSi) due to the application of PSi in solar energy harvesting [41,61-65]. PSi comprises of nanometer-sized voids containing massive hydrogenated surfaces. Relationships between porosity and refractive index have been observed, for instance:

$$n_{pc} = \left[\left(1 - \frac{p}{100} \right) (n_{dc}^2 - 1) + 1 \right]^{1/2}, \quad (7)$$

where n_{pc} , n_{dc} , and p present the dense and porous media RI and the percentage of porosity [28]. In this instance, the rate of porous film growth, solution composition, and film thickness, determines the porosity and reflectance.

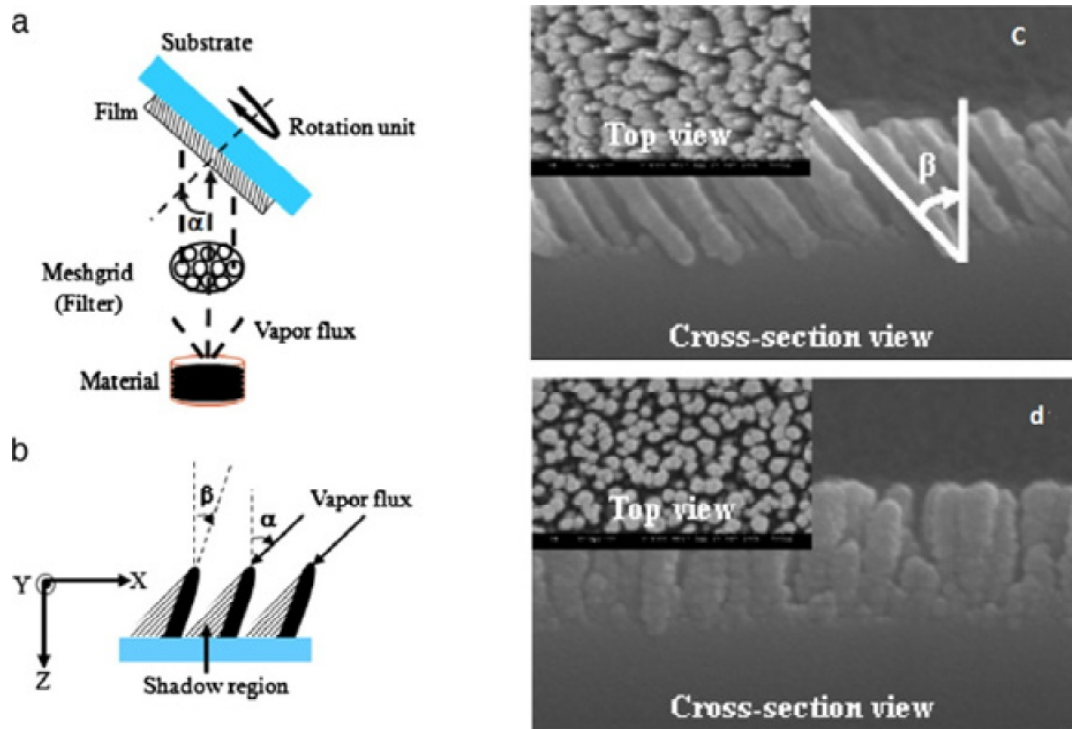


Fig. 4. (a) The schematic illustration of the GLAD technique (glancing angle deposition) and (b) column growth orientations and vapour flux with angle definitions: α represents the angle for deposition and β represents the column angle, (c) The electron micrograph scan of the nanostructured porous SiO_2 thin films which was put on stationary and (d) 0.1 rpm rotating Si (100) substrates at 85° . Reprinted with permission from K. Sobahan, Y. J. Park, J. J. Kim and C. K. Hwangbo // *Optics Communications* **284** (2011) 873.

The Glancing Angle Deposition (GLAD) technique has been used to study and fabricate the nanostructured porous SiO_2 thin films using electron-beam evaporation [66]. During the conventional GLAD method, as shown in Figs. 4a and 4b, an extra mesh grid was used. The GLAD technique with a low RI of 1.08 at wavelength of 633 nm with the deposition angle of 85° also was used to fabricate nano structured porous SiO_2 films on glass substrates. Moreover, to demonstrate the viability of this technique in multilayer optical component, a four-layer ARC consists of low-n nano structured SiO_2 film was designed and fabricated [66]. Finally, the scanning electron micrographs (SEM) of the nanostructured porous SiO_2 films onto Si substrates at an oblique angle of 85° , a result of the GLAD technique, outcomes are illustrated in in Figs. 4c and 4d.

The findings showed a high-performance anti-reflection coating recording of 99.3% transmittance and an optical absorption less than the detection limit. Furthermore, the anti-reflection coating, which is considered for standard incidence, showed an efficient result close to the incident angle of 45° . Their investigation showed a novel prospect in pro-

duction and applications of low-n nano structured SiO_2 films for photonic crystals, optical resonators, and dielectric multilayer structures with superior optical properties improved and refractive index contrasted [66].

A new process to fabricate porous structures with internal coatings was investigated by A.R. Siddiq et al. (2017) [67]. They illustrated a new process to fabricate porous structures with internal coatings, which could be achieved with the use of powder coated sacrificial porogen. The process involves the production of compositionally-gradient and multi-material coatings from the coating powder being shifted to the pore. When the pores are coated, even though the interconnectivity of the porous structure is reduced, it can be improved by decreasing the porogen powder coverage degree [67]. The high connectivity degree of the structure of the porous Polyether Ether Ketone (PEEK) is evident in Figs. 5a-5h.

The high connectivity degree for the porous PEEK structure is shown in Fig. 5a which illustrates the multiple, large windows between the pores. Fig. 5b presents the image of a porous structure which is made with beads coated with <45 nm copper pow-

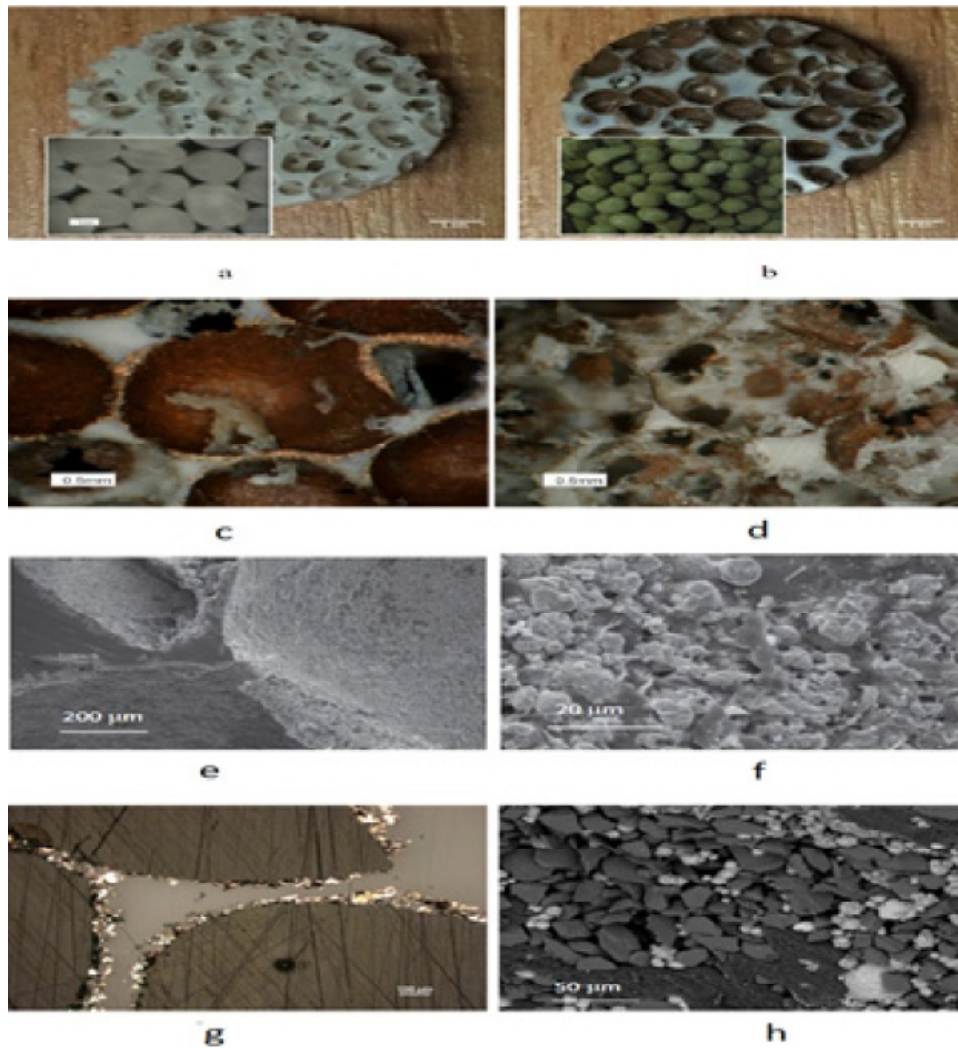


Fig. 5. a) Porous PEEK and loosely-packed salt beads (inset) and b) porous PEEK coated with Cu and (inset) Cu coated beads. Cu-coated porous structures showing increased interconnectivity as the coverage of powder decreases from c) 100% to d) 60% of the mass of Cu powder required for complete coverage. e and f) SEM images of Cu-coated porous PEEK structures showing protrusion of the Cu particles from the pore surfaces. Images of g) PEEK struts in cross section and h) cell walls, both coated with a mixture of Ni, Cu, and SiC powders. Reprinted with permission from A. R. Siddiq and A. R. Kennedy // *Materials Letters* **196** (2017) 324.

der. This structure is normally used in all the 10+ coating types investigated, as well as the image (inset) of loose Cu-coated beads. Fig. 5c illustrates the process in which the Cu coating on the beads is transferred to the PEEK cell walls during molding. Correspondingly, Fig. 5d shows the decreasing Cu powder coating level; pore interconnectivity can be increased to 60% which was measured (by mass gain) for complete coverage. Figs. 5e and 5f illustrate the secondary electron SEM images of the coating morphology. Based on the nature of the “coating” process, the pore coverage is not in the form of a continuous film; instead, the coating presents a replication of a salt bead coating by using the metal powders, which are textured and dis-

continuous. Lastly, Fig. 5g shows that the layer thickness is only evident in several particles with a high coverage level. Moreover, the different material types can be clearly differentiated through the backscattered electron image shown in Fig. 5h [67].

4.2. Biomimetic photonic nanostructures (“moth’s eye”)

The unique physical structure of moths’ eyes equips them with the ability to minimize reflection. The reduced reflections in a moth’s eye are able to determine whether they remain unseen or get eaten by a predator. Environmental pressures have caused the evolution of regular repeating prominent 3D patterns

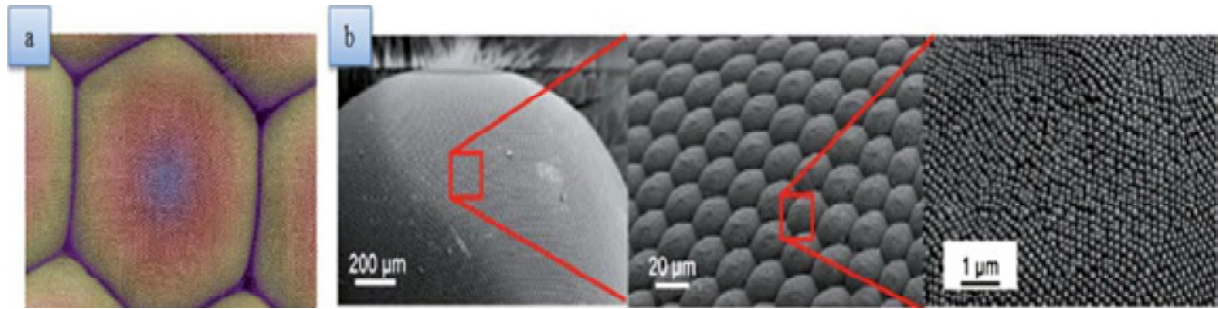


Fig. 6. (a) Image from SEM depicting little bumps on the eye of a moth, (b) SEM images that are magnified drill down illustrating the hexagonal arrangement of sub-wavelength nanostructures. Reprinted with permission from Y. Li, J. Zhang, S. Zhu, H. Dong, F. Jia, Z. Wang // *Advanced Materials* **21** (2009) 4731.

on the eye surface which could reduce reflection effectively [13,68-70]. For some insects, their camouflaging strategy; and for some nocturnal creatures, their excellent photon collection capability enables them to see in the darkness. This ability has driven scientists to investigate and analyze eye composition of nocturnal insects such as moths (Fig. 6a), butterflies and hawkmoths' transparent wings [28,71].

A similar anti-reflection effect has been achieved by scientists duplicating the 'moth eye' pattern on glass [68]. It was found that the corneal surface of moths' eyes contain nipple-arrays, which are hexagonal arrays of sub-wavelength conical or cylindrical nanostructures. Each of these protuberances diameter is obtained to be 100 nm where are 170

nm far from each other [72] (Fig. 6b). In addition to the broadband and omnidirectional AR, recent research now has shown that butterfly eyes are extremely sensitive to polarized light; furthermore, the nanostructures could remove the disparities in the reflection of polarized lights. This is because the light had lost the distinct boundary between the glass and the air, or the moth eyes and the air. The transition now happens over an appreciable wavelength fraction, instead of the very sharp boundary between glass and air. As the reflections can only occur when the reflections are drastically reduced and there is a change in index of fraction and a longer a sharp boundary in between the materials [68], it is noteworthy that the microstructure's size is important; moth eyes contain a regular repeating pattern of

Table 4. A summary of biomimetic photonic nanostructures ARC outcomes.

Ref	Year	Materials	Description
[73]	2014	polystyreneblock-poly(methyl methacrylate) (PS-b-PMMA)	Via the application of this coating material, they have improved the device fill factor from 70% to 71%.
[74]	2014	poly(3-hexylthiophene-2,5-diyl):indene-C60 bis-adduct (P3HT:ICBA)	A 24.3% rise in photocurrent is obtained without ignoring dark electrical characteristics.
[75]	2011	polymethyl methacrylate (PMMA)	The modification in structure is decreased the reflection of solar cell from 13.2% to 7.8%. The PMMA also helps to improve power conversion efficiency around 1.35% up to 14.2%.
[76]	2010	polystyrene nanosphere	The cell conversion efficiency with sub-wavelength structure is improved by 46.1% compared to bare cells and 3.4% in comparison to SL ARC.
[77]	2012	nanostructured ZnO	The reflection of the surface from polished silicon is suppressed in wavelengths between 400 to 900 nm from 30.8% down to 10.6% via micro-scale pyramidal surface texturing. And after applying the ZnO nanostructure on the textured silicon, it is reduced to 3.4%.

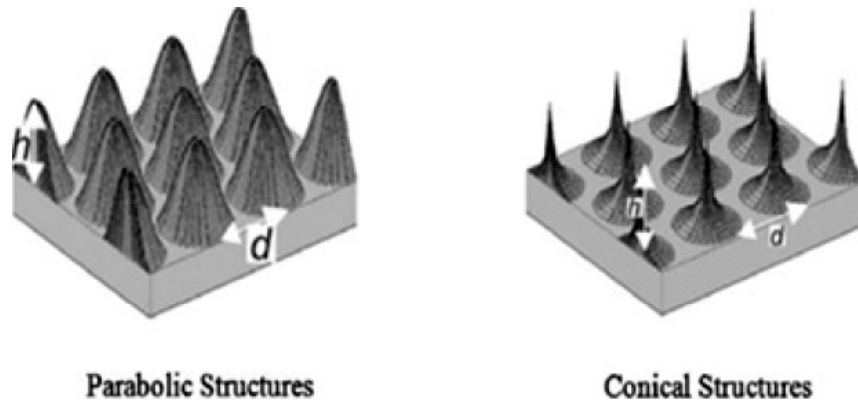


Fig. 7. Gaussian-bell shape, conical, and paraboloidal on the cornea of amber. Reprinted with permission from S. A. Boden and D. M. Bagnall // *Applied Physics Letters* **93** (2008) 133108.

hexagonal finger-like projections which rise about 200 nm from the eye's surface and are spaced roughly 300 nm from each other. This size of the microstructure is roughly optimized for antireflection of the visible spectrum; hence, the surface can be optimized to reflect shorter or longer wavelengths, respectively by making the structures smaller or larger [68]. Table 4 summarises research that has been conducted on other biomimetic photonic nanostructures anti-reflection based on the efficiency, transmittance and reflection.

Further investigation showed that the nanostructures contain the gradient RI between the ambient (RI 1.0) and chitin (polysaccharide RI 1.54, consider substrate) [78]. This illustrates that AR is mainly caused by the Rayleigh effect, which shows exceptional transmission. Lithography was used for the initial reproduction of the structure's "moth's eye", which comprised of three gratings crossing at 120° [28]. Thus, highly precise moth's eye" arrays were produced through electron-beam etching based on the requirements for scalability and precision. Boden et al. (2006) presented a very intriguing finding based on the analysis of day-time anti-reflectivity and computationally illustrated that moth eye structures with 250 nm have the same performance as double-layer ARCs [79]. However, a 500 nm increase in thickness could decrease the loss of the reflection by 2. Consequently, the additional photon collection caused a 12% rise in solar cell energy. Fig. 7 shows the Gaussian-bell shape, conical, and paraboloidal on the cornea of amber.

The intensive probe of other species' eyes, such as in amber cornea revealed sinusoidal gratings of 250 nm periodicity, which shows excellent broadband properties. Other studies have also analyzed different moth's eye nipple array profiles [81] which are , Gaussian-bell shape, conical, and

paraboloidal (Fig. 7). Additional studies have reported that the best performance is demonstrated by paraboloidal nipple array displays. Consequently, they proposed that the optimal decrease of reflectance could be achieved with tall paraboloids with bases that touch each other at the hemispherical facet surface [81]. An intensive study of the 361 corneal samples from different species [28] had stipulated that instead of the moth eye, ($< \lambda/2$), moth's eye structures shape, and the inter-nipple spacing have played a critical role. This idea was expanded onto fused silica substrate and quartz containing conical array which could reduce reflectance to 0.5% when the wavelength range is 400–800 nm in polymer, and, amongst other materials, GaSb [82]. In this regard, after comparing with multi-layer thin films in previous discussions, the study found that the sub-wavelength structure (SWS) possesses exceptional compatibility with the substrate material. Meanwhile, the use of the latter has caused issues in adhesion as a result of the difference between the thermal coefficients of the substrate with the layer located either beside it, or between the layers. Moreover, previous research such as [83], conducted RCWA (solutions to Maxwell equations) over EMT or rigorous coupled wave analysis, where the wave analysis offers better optimization as it was able to produce a more effective prediction of the significant parameters.

4.3. Textured surface ARCs

The creation of suitable surface profiles (texturing) could improve AR properties [84,85]. The rendering of antireflective substrates has been demonstrated since the 1960s through surface texturing [86,87]. To produce highly efficient solar cells, Syed A.M. Said et al. (2015) reported how ARC of PV module,

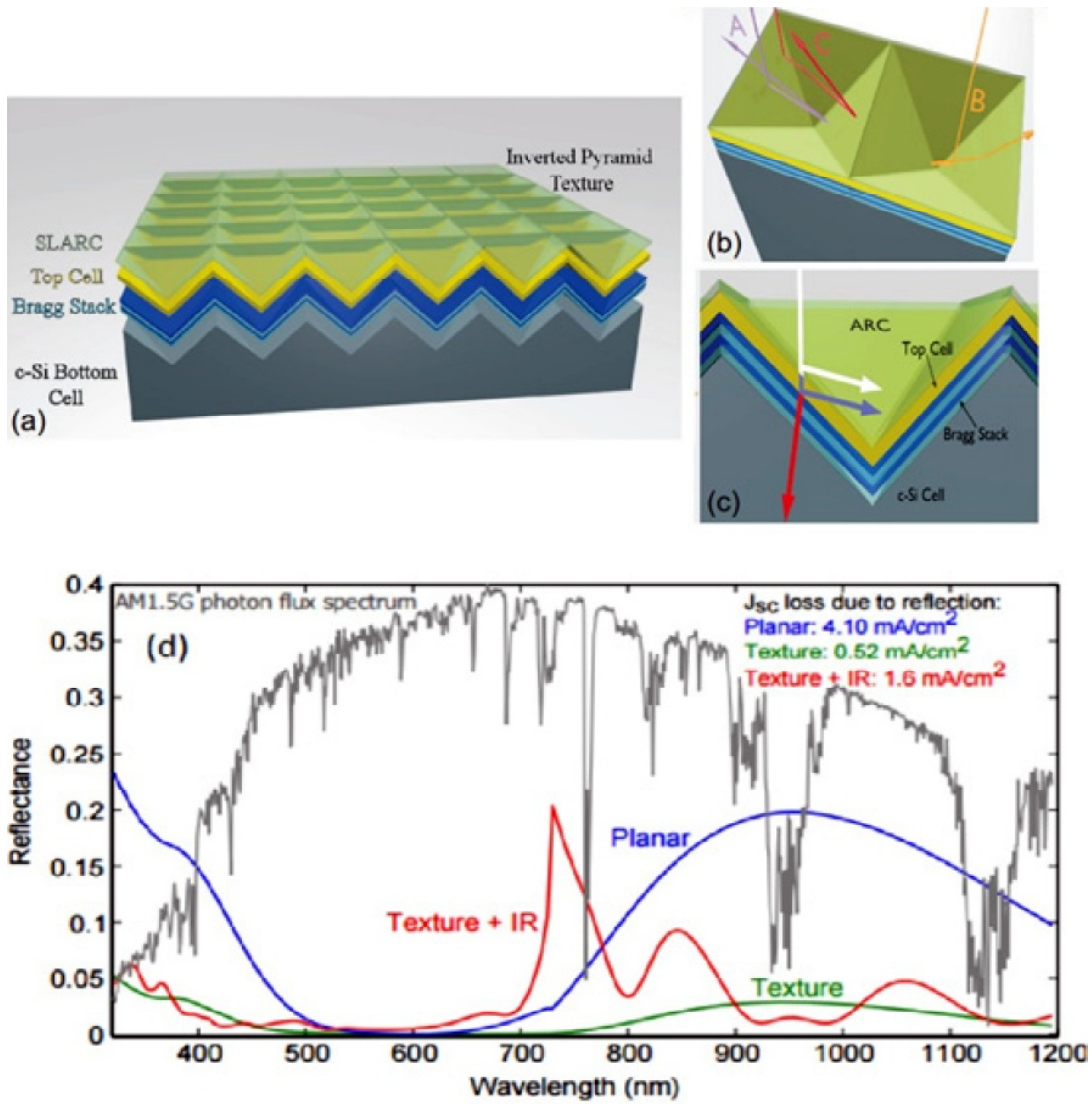


Fig. 8. (a) Textured surface wide-angle view which shows the cross-sectional conformal deposition of the layers. (b) Three possible inverted pyramid texture light paths for. (c) The schematic internal optical structure cross-section of: the intermediate reflector transfers not high energy light into the bottom c-Si cell (red arrow), reflects short wavelength goes into the top cell (indigo arrow). (d) Front-surface reflectance and equivalent reflected J_{sc} for each structure. A normalized AM1.5G solar band is illustrated in gray colour for reference. Reprinted with permission from B. W. Schneider, N. N. Lal, S. Baker-Finch and T. P. White // *Optics express* **22** (2014) A1422.

glass support, and texturing affect the modules' total performance of modules [88,89]. According to the results of this study, the module surface texturing and the addition of an anti-reflective coating increased the clean photovoltaic module power output, with a mean of between 4% and 8%. An anti-reflective coating covers the clean modules which exhibit the highest increase of power output. The module surface texturing normally increased the temperature based on the flat glass modules. The results of the study affirm the reduction of 10–17%; the PV module power output was exposed for six

weeks without being cleaned as a result of dust accumulation. Thus, the presence of dust on the PV modules glass cover's anti-reflective coating and texturing had caused a reduction in power [88,90].

A practical tandem cell structure was introduced by Bennett W. Schneider et al. (2014). This combines the common pyramidal surface texturing on the Si bottom cell, which contains the wavelength-selective intermediate reflector [91]. The tandem cell geometry, as shown in Figs. 8a-8c, was proposed in the study. Here, the thin-film top cell is conformally deposited onto a c-Si cell which is a pyramidally-

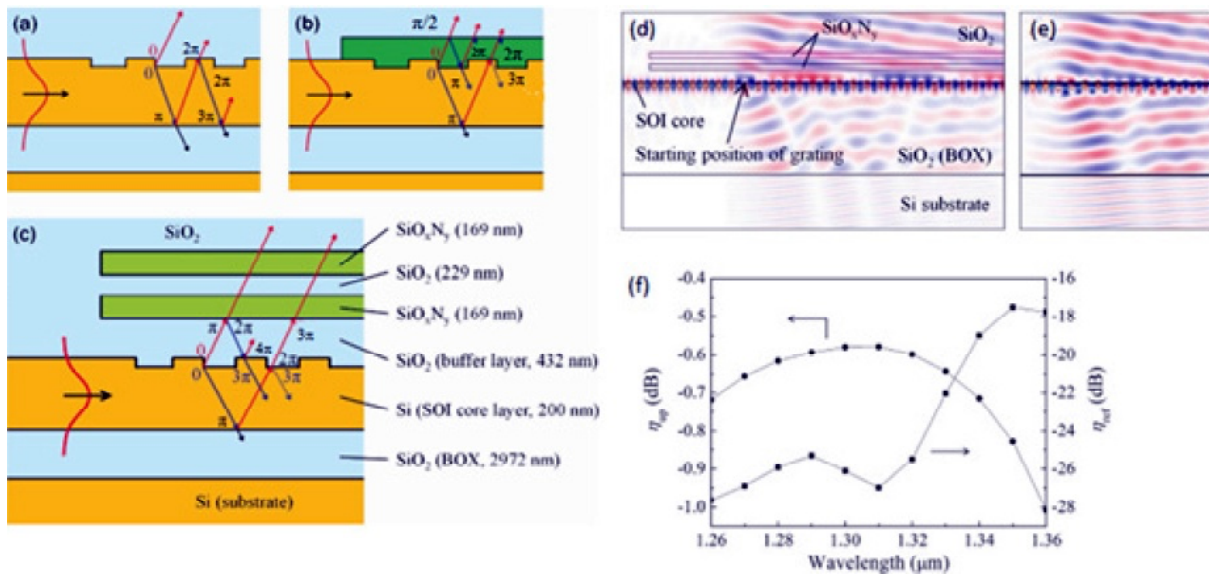


Fig. 9. Cross-sections for (a) a single-layer grating (b) a double-layer grating, and (c) a quadruple-layer grating of ARC. The upward and downward propagating lights were respectively represented by the red and blue arrows. The lights have relative phases at the layer interfaces. The transverse electric field spreading of light distributing in and out of gratings (d) with a quadruple ARC and (e) without a quadruple ARC. (f) Presents the wavelength dependence of upward directionality (solid circle) and back reflection along the waveguide (solid square) with a quadruple ARC. Reprinted with permission from M. Tokushima, J. Ushida, T. Uemura and K. Kurata // *Applied Physics Express* **8** (2015) 092501.

textured incorporating the intermediate Bragg reflector among the cells. The method is able to portray the Bragg reflector design and the combined texture which can obtain an efficiency of around 4%, in comparison to a planar tandem cell.

Meanwhile, Fig. 8d presents the fact that the planar top cell shows weak absorption at wavelengths $500 \text{ nm} < \lambda < 730 \text{ nm}$, the loss of reflection at short wavelengths ($\lambda < 500 \text{ nm}$), while the bare Si bottom cell effects a substantial reflection reduction at wavelengths $\lambda > 800 \text{ nm}$. The combined reflection is reduced for the planar cell similar to a short current reduction of 4.1 mA cm^{-2} under the illumination AM1.5G (the G stands for global that contains direct and diffuse radiation) [91].

The combination of a selective intermediate reflector and these surfaces can provide substantial light-trapping in the top cell. In this research, an all-planar tandem cell with a SLARC on the front with no intermediate reflector is considered first. The study had achieved 1% conventional monocrystalline c-Si cells across the solar spectrum. This was achieved through combining the pyramidal surface texturing and the dielectric anti-reflection coating, as illustrated by the crystallographic planes of the Si (111) structure, indicating a high anti reflection quality. The low reflectance could be caused by dif-

ferent reflections from the pyramidal surfaces, as shown in Fig. 9. For the light trapping in thin film cells, similar textures were used to deposit the absorbing layer onto pyramidal or v-groove textured substrates [92-94]. According to Sai et al. (2015) report, a proper light-trapping texture should be combined with the sub-wavelength structure to increase the absorption of thin-film silicon solar cells. Consequently, the increase in the microcrystalline silicon cell short-circuits current density from 29.1 to 30.4 mA/cm^2 in a designated area of 1 cm^2 , illustrates the effectiveness of dielectric films with sub-wavelength structures [95].

4.4. Anti-reflection grating (ARG)

The broadband anti-reflection obligation for a wide area which can reach up to $0.1\text{--}10 \text{ THz}$, (terahertz) in the wavelength of $0.30 \text{ }\mu\text{m}$ to 3 mm [96], can be contended using the ARGs [97,98]. Hence, the grating structures possess a similar principle to the creation of a constant gradient of refractive index n_s , to ambient 1. ARG efficiency was proven through THz [28] wavelength and solar [99] microwave ranges. However, ARGs were found to have less solar cell efficiency as the gratings do not cater to higher diffraction orders propagating the zero diffrac-

Table 5. A summary of some grating ARC reports.

Ref	Year	Materials	Description
[97]	2017	Two-Dimensional rectangular grating on the GaSb surface	The grating structure with optimal parameters leads an average of 75.4% improvement in the output power when the temperature was in the range of 1000–1800 K. At the maximum temperature, the conversion efficiency increased to 24.8%.
[98]	2017	Si ₃ N ₄ /SiO ₂ bilayer grating structure	Using this method, a grating coupler with in-plane coupling efficiency of 66% and up-reflection of only 3.6% is obtained
[102]	2017	Anodic aluminum oxide (AAO) nanogratings	Researchers found an increase of short-circuit current density (1.32 mA/cm ²) with SiN _x :H/AAO complex coating. The relative power conversion efficiency obtains a growth of around 2.2% points
[103]	2014	fused silica transmission gratings	The transmitted order diffraction efficiency raised to 96% at 800 nm
[104]	2013	SiO ₂ and Ta ₂ O ₅	Researches produced a grating with 1740 grooves/mm applying an ARC. An efficiency increase equal to 7% from 92% is obtained.
[105]	2012	a double-sided grating design SiO ₂ /Si	Researches have achieved a decrease from 34.63% to 33.86 mA/cm ² in short-circuit photocurrent.

tion orders for both reflected and directly transmitted lights. This inherently contributes to the entire collected energy in a solar cell [28].

Following an investigation into two dimensional (2D) rectangular gratings on a GaSb surface, Haitong Yu et al. (2017) found that the gratings can create “AR” patterns for nano-gap thermophotovoltaic devices [100]. This could considerably improve the near-field radiative flux obtained from the emitter to a GaSb cell and enhance the conversion and output power efficiency. The study presented a 200-nm gap in thermophotovoltaic (TPV) power generation arrangement containing a GaSb cell and a planar infrared plasmonic emitter. The study also included a rigorous coupled-wave analysis to calculate the spectral near-field radiative flux using the periodic structure. Moreover, in regards to coupling to a multimode fiber, Masatoshi Tokushima et al (2015) presented the design of an optimized thin grating coupler design of a silicon-on-insulator wafer with a quadruple ARC; this included multiple layers of SiO_xN_y and SiO₂. This designed ARC could generate the sufficient destructive interference downward emission, whilst maintaining the upward emission constructive interference [101]. Fig. 9a demonstrates the returned light reflecting downward from the bared media on the main top surface. As a result, it interferes constructively with the primarily downward diffracted light, simultaneously reducing the light emitted upward and improving the light emitted downward.

Figs. 9b and 9c represent the least complicated ARCs. Here, the single and double dielectric layers are put at the top of the core surface. In this case, the ARC cannot be optimized if the light is initially diffracted upward by the grooves, but it will be optimized when the light travels up from the bottom of the core; hence, as shown in Fig. 9b, the light that is initially diffused will be partially reflected to the bottom at the ARC layer top surface. Fig. 9d shows that the Si substrate is emitted downward, lower than the upward emission into the SiO₂ upper cladding. The 2D Finite Difference Time Domain (FDTD) technique has been applied for simulating the grating operation with the quadruple ARC. Meanwhile, Fig. 9d illustrates the electric field propagation of light surrounding the grating, whilst Fig. 9e shows grating field distribution minus the ARC, and Fig. 9f shows the wavelength dependence of the upward directionality “ ζ ” up evaluated in the “O band” (1.26-1.36 μ m wavelength). This study numerically confirms the grating upward directionality, which can reach up to 0.58% decibels (dB). As the ARC is far from the Silicon On Insulator (SOI) core layer and the shallow grating, the input waveguide back reflection could be suppressed to 27% dB [101]. Lei Wu et al (2017) experimentally applied Anodic aluminum oxide (AAO) nano gratings to polycrystalline silicon (pc-Si) solar cells at front surface to enhance the light coupling [102]. The study illustrates an enhancement of the short-circuit current density (1.32 mA/cm²) together with the

complex coating of $\text{SiN}_x\text{:H/AAO}$; a growth of approximately 2.2% points was observed in the relative power conversion efficiency.

Table 5 summarises the other studies previously carried out on Anti-reflection grating based on efficiency, transmittance and reflection. Research of antireflection coatings (materials and methods) are still in their infancy; their stability, structure and types of coating layers should be given more consideration. In addition, their thinness and low material cost are crucial factors which make them suitable for future industrial use. Furthermore, the study also discussed the different forms of antireflection coating in.

5. CONCLUSION

This review has provided a categorized investigation into the current ARC materials, which may assist researchers in selecting the best ARC material to suit their designed applications; particularly in solar cells. So far, various researches have presented the reflection performance of different coating types and antireflection coating designs that can be separated in two major sections. Firstly, this is based on the layer composition that includes: (1) Single layer ARCs by quarter-wavelength, the biggest challenge for single-layer coatings is the decrease in the reflectivity for partial wavelengths. (2) Double-layer and multilayer ARCs, several attempts have been made to minimize the overall reflected vectors summation; it has been found that this can be done by making an adjustment to the film thickness and the RI. (3) Gradient refractive index ARCs; these have a lower reflectance in 430–1200 nm range compared to double-layer ARCs. Secondly, this is based on the surface topography which includes: (1) Porous ARCs which showed a high-performance anti-reflection coating where it recorded 99.3% transmittance. (2) Biomimetic nanostructures that are extremely sensitive to polarized light. (3) Textured surface ARCs which can significantly improve the ARC properties by a suitable surface texturing. (4) Anti-reflection gratings those are suitable for the broadband anti-reflection obligation in a wide area. This hinders the improvement of performance to cater for the demand of optoelectronic devices because of the rapid advancement in nanophotonics and nanofabrication that calls state-of-the-art ARCs that are iridescent free, ultra thin and broadband. One major particular concern is the invention of durable, efficient and inexpensive materials for ARCs that can be used for different electronic and optical equipment. Among all ARCs which have been of great

interest to researchers in recent years, a 2D rectangular grating has improved the absorption of light on GaSb surfaces remarkably. Nevertheless, the application of grating ARCs on a group of III-V semiconductors as absorbers has not yet been well addressed; this can be compatible future work in this field.

ACKNOWLEDGEMENT

The authors are thankful to the Universiti Teknologi PETRONAS (UTP) for their financial aid provided via the YAYASAN Universiti Teknologi PETRONAS (YUTP) grant (No-0153AA-A96).

REFERENCES

- [1] M. Keshavarz Hedayati and M. Elbahri // *Materials* **9** (2016) 497.
- [2] H. Hanaei, M. K. Assadi and R. Saidur // *Renewable and Sustainable Energy Reviews* **59** (2016) 620.
- [3] K. P. Lim, D. K. Ng and Q. Wang // *Journal of Physics D: Applied Physics* **49** (2016) 085302.
- [4] S. De Wolf, A. Descoedres, Z. C. Holman and C. Ballif // *Green* **2** (2012) 7.
- [5] J. Cai and L. Qi // *Materials Horizons* **2** (2015) 37.
- [6] L. Yao and J. He // *Progress in Materials Science* **61** (2014) 94.
- [7] J. van de Groep, P. Spinelli and A. Polman // *Nano letters* **15** (2015) 4223.
- [8] E. Shi, H. Li, L. Yang, L. Zhang, Z. Li and P. Li // *Nano letters* **13** (2013) 1776.
- [9] B. Zhang, J. Hendrickson, N. Nader, H.-T. Chen and J. Guo // *Applied Physics Letters* **105** (2014) 241113.
- [10] R. Maas, S. A. Mann, D. L. Sounas, A. Alu, E. C. Garnett and A. Polman // *Physical Review B* **93** (2016) 195433.
- [11] M. L. Brongersma, Y. Cui and S. Fan // *Nature materials* **13** (2014) 451.
- [12] M. Suzuki, A. Takada, T. Yamada, T. Hayasaka, K. Sasaki and E. Takahashi // *Thin Solid Films* **519** (2011) 8485.
- [13] H. Cui, S. Pillai, P. Campbell and M. Green // *Solar Energy Materials and Solar Cells* **109** (2013) 233.
- [14] T. C. Choy, *Effective medium theory: principles and applications*, vol. 165 (Oxford University Press, 2015).
- [15] F. Padera, *Measuring Absorptance (k) and Refractive Index (n) of Thin Films with the PerkinElmer Lambda 950/1050 High*

- Performance UV-Vis/NIR Spectrometers* (PerkinElmer Inc., Application note, UV/Vis Spectroscopy, 2013).
- [16] G. K. Mor, K. Shankar, M. Paulose, O.K. Varghese and C. A. Grimes // *Nano letters* **6** (2006) 215.
- [17] D. Janczak, M. Słoma, G. Wróblewski, A. Młodziak and M. Jakubowska // *Sensors* **14** (2014) 17304.
- [18] E. Shi, L. Zhang, Z. Li, P. Li, Y. Shang and Y. Jia // *Scientific reports* **2** (2012) 884.
- [19] M. K. Assadi and J. S. Appasamy // *International Journal of Renewable Energy Research (IJRER)* **6** (2016) 1612.
- [20] T. Feng, D. Xie, Y. Lin, Y. Zang, T. Ren and R. Song // *Applied physics letters* **99** (2011) 233505.
- [21] J. Moghal, J. Kobler, J. R. Sauer, J. Best, M. Gardener and A. A. Watt // *ACS applied materials & interfaces* **4** (2012) 854.
- [22] B.-T. Liu and W.-D. Yeh // *Colloids and Surfaces A: Physicochemical and Engineering Aspects* **356** (2010) 145.
- [23] Y. Song, X. Li, C. Mackin, X. Zhang, W. Fang and T. S. Palacios // *Nano letters* **15** (2015) 2104.
- [24] N. Sultanova, S. Kasarova and I. Nikolov // *Acta Physica Polonica-Series A General Physics* **116** (2009) 585.
- [25] G. Beadie, M. Brindza, R. A. Flynn, A. Rosenberg and J. S. Shirk // *Applied optics* **54** (2015) F139.
- [26] Y.-J. Lee, D.S. Ruby, D.W. Peters, B.B. McKenzie and J. W. Hsu // *Nano letters* **8** (2008) 1501.
- [27] X. Gan, R. Lv, H. Zhu, L.-P. Ma, X. Wang and Z. Zhang // *Journal of Materials Chemistry A* **4** (2016) 13795.
- [28] H. K. Raut, V. A. Ganesh, A. S. Nair, and S. Ramakrishna // *Energy & Environmental Science* **4** (2011) 3779.
- [29] A. Szeghalmi, M. Helgert, R. Brunner, F. Heyroth, U. Gösele and M. Knez // *Applied optics* **48** (2009) 1727.
- [30] A. Bahrami, S. Mohammadnejad, N. J. Abkenar and S. Soleimaninezhad // *International Journal of Renewable Energy Research (IJRER)* **3** (2013) 79.
- [31] F. Zhan, Z. Li, X. Shen, H. He and J. Zeng // *The Scientific World Journal* **2014** (2014) 100.
- [32] I. G. KAVAKLI and K. Kantarli // *Turkish Journal of Physics* **26** (2002) 349.
- [33] S. Lee, S. Choi and J. Yi // *Thin Solid Films* **376** (2000) 208.
- [34] D. N. Wright, E. S. Marstein and A. Holt, In: *Photovoltaic Specialists Conference* (IEEE, 2005), p. 1237.
- [35] S. K. Dhungel, J. Yoo, K. Kim, S. Jung, S. Ghosh and J. Yi // *Journal of the Korean Physical Society* **49** (2006) 885.
- [36] Y. Li, Y. Zhang, and X. Liu // *Optical Interference Coatings journal, OSA Publishing* **5** (2013), p. WC. 5.
- [37] K. Ali, S. A. Khan, and M. M. Jafri // *International Journal of Electrochemical Science* **9** (2014) 7865.
- [38] J. Sun, X. Cui, C. Zhang, C. Zhang, R. Ding and Y. Xu // *Journal of Materials Chemistry C* **3** (2015) 7187.
- [39] L. Lancellotti, E. Bobeico, A. Capasso, E. Lago, P. D. Veneri and E. Leoni // *Solar Energy* **127** (2016) 198.
- [40] S. Musalinov, A. Anzulevich, I. Bychkov, A. Gudovskikh and M. Shvarts // *Semiconductors* **51** (2017) 88.
- [41] E. Osorio, R. Urteaga, L. N. Acquaroli, G. García-Salgado, H. Juaréz and R. Koropecski // *Solar Energy Materials and Solar Cells* **95** (2011) 3069.
- [42] S. Saylan, T. Milakovich, S.A. Hadi, A. Nayfeh, E.A. Fitzgerald and M.S. Dahlem // *Solar Energy* **122** (2015) 76.
- [43] S. J. Oh, S. Chhajed, D. J. Poxson, J. Cho, E. F. Schubert and S. J. Tark // *Optics express* **21** (2013) A157.
- [44] A. Uzum, M. Kuriyama, H. Kanda, Y. Kimura, K. Tanimoto and H. Fukui // *International Journal of Photoenergy* **2017** (2017).
- [45] H. Yao, Z. Chen and T. Chang, In *Proc. 40th International Conference Infrared, Millimeter, and Terahertz waves* (2015), p. 1.
- [46] X. Li, X. Hu, Y. Li and L. Chai // *Journal of Lightwave Technology* **32** (2014) 1463.
- [47] C. Xiong, W. Xu, Y. Zhao, J. Xiao and X. Zhu // *Modern Physics Letters B* **31** (2017) 1740028.
- [48] L. Huang, Q. Jin, X. Qu, J. Jin, W. Yang, L. Wang // *Surface and Coatings Technology* **320** (2017) 82.
- [49] L. Huang, Q. Jin, X. Qu, J. Jin, C. Jiang and W. Yang // *Superlattices and Microstructures* **96** (2016) 198.
- [50] M. Choi, J. W. Leem and J. S. Yu // *RSC Advances* **5** (2015) 25616.

- [51] M.-T. Tsai, Z.-P. Yang, T.-S. Jing, H.-H. Hsieh, Y.-C. Yao and T.-Y. Lin // *Solar Energy Materials and Solar Cells* **136** (2015) 17.
- [52] B. Li, P. Xie, W. Su, X. Ma, H. Luo and D. Liu // *Materials & Design* **107** (2016) 302.
- [53] Z. Ge, P. Rajbhandari, J. Hu, A. Emrani, T.P. Dhakal and C. Westgate // *Applied Physics Letters* **104** (2014) 101104.
- [54] Y. Zhang, C. Li and M. Loncar // *Optics letters* **38** (2013) 646.
- [55] U. Schulz, P. Munzert, S. Reinhard, F. Rickelt, H. Knopf and C. Weber // *Optical Interference Coatings*, OSA Publishing **3** (2016), p. FB. 5.
- [56] H. Shen and C. Zhao // *Thin Solid Films* **542** (2013) 204.
- [57] J. Dobrowolski, D. Poitras, P. Ma, H. Vakil and M. Acree // *Applied optics* **41** (2002) 3075.
- [58] M. Brophy, M. K. Trubetskov, P. Kupinski and J. Watson, *Optical Interference Coatings*, OSA Publishing **8** (2016), p. ThD. 6.
- [59] N. Denisova // *Radiophysics and Quantum Electronics* **59** (2016) 234.
- [60] K. Q. Salih and N. Ahmed // *International Journal Nanoelectronics and Materials* **1** (2009) 109.
- [61] R. Chaoui, B. Benyahia and Y. Si Ahmed // *International Journal of Engineering Research in Africa* (2016) 1.
- [62] V. Yerokhov and O. Ierokhova, In: *Proc. Electronics and Information Technology (EIT), 2016 International Conference*, p. 1.
- [63] W. J. Aziz, A. Ramizy, K. Ibrahim, Z. Hassan and K. Omar // *Optik-International Journal for Light and Electron Optics* **122** (2011) 1462.
- [64] J. Selj, A. Thøgersen, S. Foss and E. Marstein // *Journal of Applied Physics* **107** (2010) 074904.
- [65] M. Elshorbagy, K. Abdel-Hady, H. Kamal and J. Alda // *Optics Communications* **390** (2017) 130.
- [66] K. Sobahan, Y.J. Park, J.J. Kim and C.K. Hwangbo // *Optics Communications* **284** (2011) 873.
- [67] A. R. Siddiq and A. R. Kennedy // *Materials Letters* **196** (2017) 324.
- [68] M. Fink, *Types of Anti-Reflective Treatments and When to Use Them* (The Photonics Solutions Update, 2015).
- [69] J. Xu and Z. Guo // *Journal of colloid and interface science* **406** (2013) 1.
- [70] Y. Chen, A. Santos, Y. Wang, T. Kumeria, J. Li and C. Wan // *ACS applied materials & interfaces* **7** (2015) 19816.
- [71] W. Yi, D.-B. Xiong and D. Zhang // *Nano Advances* **1** (2016) 62.
- [72] Y. Li, J. Zhang, S. Zhu, H. Dong, F. Jia, Z. Wang // *Advanced Materials* **21** (2009) 4731.
- [73] A. Rahman, A. Ashraf, H. Xin, X. Tong, P. Sutter and M. D. Eisaman // *Nature communications* **6** (2015) 5963.
- [74] J. D. Chen, L. Zhou, Q. D. Ou, Y. Q. Li, S. Shen and S. T. Lee // *Advanced Energy Materials* **4** (2014) 1301777.
- [75] J. Chen, W.-L. Chang, C. Huang and K. Sun // *Optics express* **19** (2011) 14411.
- [76] M. Chiu, F. Chang, C. Chang, M. Tsai and P. Yu, In: *Photovoltaic Specialists Conference* (IEEE, 2010) 000471.
- [77] S.-Y. Han, B. K. Paul and C.-H. Chang // *Journal of Materials Chemistry* **22** (2012) 22906.
- [78] A. R. Parker and H. E. Townley // *Nature nanotechnology* **2** (2007) 347.
- [79] S. A. Boden and D. M. Bagnall, In: *Photovoltaic Energy Conversion, Conference Record* (IEEE, 2006), p. 1358.
- [80] S. A. Boden and D. M. Bagnall // *Applied Physics Letters* **93** (2008) 133108.
- [81] D. Stavenga, S. Foletti, G. Palasantzas and K. Arikawa // *Proceedings of the Royal Society of London B: Biological Sciences* **273** (2006) 661.
- [82] W.-L. Min, A. P. Betancourt, P. Jiang and B. Jiang // *Applied Physics Letters* **92** (2008) 141109.
- [83] S. A. Boden and D. M. Bagnall // *Progress in Photovoltaics: Research and Applications* **18** (2010) 195.
- [84] L. Dobrzański and M. Szindler // *Journal of Achievements in Materials and Manufacturing Engineering* **52** (2012) 7.
- [85] L. Dobrzański, A. Dryga, P. Panek, M. Lipiński and P. Zięba // *Archives of Materials Science* **6** (2009) 6.
- [86] V. V. Iyengar, B. K. Nayak and M. C. Gupta // *Solar Energy Materials and Solar Cells* **94** (2010) 2251.
- [87] M. G. Salvaggo, R. Passalacqua, S. Abate, S. Perathoner, G. Centi and M. Lanza // *Solar Energy* **125** (2016) 227.
- [88] S. A. Said, N. Al-Aqeeli and H. M. Walwil // *Solar Energy* **113** (2015) 295.

- [89] A. Ingenito, O. Isabella and M. Zeman // *Progress in Photovoltaics: Research and Applications* **23** (2015) 1649.
- [90] Y. Sun, S.-C. Wu and B. Yan // *Physical Review B* **92** (2015) 115428.
- [91] B. W. Schneider, N. N. Lal, S. Baker-Finch and T. P. White // *Optics express* **22** (2014) A1422.
- [92] S.J. Kim, G.Y. Margulis, S.-B. Rim, M.L. Brongersma, M.D. McGehee and P. Peumans // *Optics express* **21** (2013) A305.
- [93] M. Jong, P. Sonneveld, J. Baggerman, C. Rijn, J. Rath and R. Schropp // *Progress in Photovoltaics: Research and Applications* **22** (2014) 540.
- [94] S.-B. Rim, S. Zhao, S.R. Scully, M.D. McGehee and P. Peumans // *Applied Physics Letters* **91** (2007) 243501.
- [95] H. Sai, T. Matsui, K. Saito, M. Kondo and I. Yoshida // *Progress in Photovoltaics: Research and Applications* **23** (2015) 1572.
- [96] Y. Wang, L. Chen, H. Yang, Q. Guo, W. Zhou and M. Tao // *Solar Energy Materials and Solar Cells* **93** (2009) 85.
- [97] H. Yu, D. Liu, Z. Yang and Y. Duan // *Scientific Reports* **7** (2017) 1026.
- [98] Z. Zhang, B. Huang, Z. Zhang, C. Cheng, H. Liu, H. Li // *Optics & Laser Technology* **90** (2017) 136.
- [99] K. Wang and D. M. Mittleman // *JOSA B* **22** (2005) 2001.
- [100] H. Yu, D. Liu, Z. Yang and Y. Duan // *Scientific reports* **7** (2017) 1026.
- [101] M. Tokushima, J. Ushida, T. Uemura and K. Kurata // *Applied Physics Express* **8** (2015) 092501.
- [102] L. Wu, H. Zhang, F. Qin, X. Bai, Z. Ji and D. Huang // *Optics Communications* **385** (2017) 205.
- [103] X. Chen, C. Li, L. Liu, L. Li, J. Wu and Z. Chang // *SPIE/COS Photonics Asia* (2014) 92661N.
- [104] K. Nagashima, A. Kosuge, Y. Ochi and M. Tanaka // *Optics express* **21** (2013) 18640.
- [105] K. X. Wang, Z. Yu, V. Liu, Y. Cui and S. Fan // *Nano letters* **12** (2012) 1616.